

<https://doi.org/10.1038/s42003-024-06268-5>

Growth phase-dependent reorganization of cryptophyte photosystem I antennae

Check for updates

Shumeng Zhang^{1,3}, Long Si^{1,2,3}, Xiaodong Su¹, Xuelin Zhao¹, Xiaomin An¹ & Mei Li¹✉

Photosynthetic cryptophytes are eukaryotic algae that utilize membrane-embedded chlorophyll *a/c* binding proteins (CACs) and lumen-localized phycobiliproteins (PBPs) as their light-harvesting antennae. Cryptophytes go through logarithmic and stationary growth phases, and may adjust their light-harvesting capability according to their particular growth state. How cryptophytes change the type/arrangement of the photosynthetic antenna proteins to regulate their light-harvesting remains unknown. Here we solve four structures of cryptophyte photosystem I (PSI) bound with CACs that show the rearrangement of CACs at different growth phases. We identify a cryptophyte-unique protein, PsaQ, which harbors two chlorophyll molecules. PsaQ specifically binds to the luminal region of PSI during logarithmic growth phase and may assist the association of PBPs with photosystems and energy transfer from PBPs to photosystems.

Oxyphototrophic organisms sustain most of the life forms on earth by absorbing solar energy and converting it into the chemical energy and releasing oxygen. Photosystems I and II (PSI and PSII) are two thylakoid membrane-embedded complexes essential for the photosynthetic light reactions. Both photosystems contain a structurally conserved core complex and a highly variable antenna system. The antenna proteins increase the light harvesting capability of the photosystem core where the charge separation occurs. While most eukaryotic phototrophs utilize the membrane-embedded light-harvesting complexes (LHCs) as peripheral antennae for both photosystems, prokaryotic cyanobacteria contain huge membrane-extrinsic phycobilisomes (PBSs) serving as the antenna system of PSII^{1–3}. Red algae possess both PBSs and LHCs as antennae for PSII and PSI, respectively^{4,5}. The variable antenna systems allow the efficient photosynthesis of different organisms, and are essential for them to adapt to their respective habitats⁶.

Photosynthetic cryptophytes are unicellular organisms that acquired their chloroplasts from red algae by secondary endosymbiosis millions years ago⁷. These microalgae utilize both membrane-embedded LHCs and membrane-extrinsic phycobiliproteins (PBPs) as antennae⁸. However, PBPs in cryptophytes form rhombic $\alpha 1\alpha 2\beta\beta$ -tetramers^{9,10} and are located at the thylakoid lumen¹¹, differing from the stroma-localized disk-shaped PBPs in cyanobacteria and red algae, which are usually composed of three $\alpha\beta$ -heterodimers¹. Cryptophyte LHCs are similar to those in red algae and diatom, but contain unique carotenoid alloxanthin, as well as chlorophyll (Chl) *a* and *c2*, thus were named ACP (alloxanthin and chlorophyll *a/c*

binding protein)¹² or more generally termed CAC (chlorophyll *a/c* binding protein)¹³.

Cryptophyte algae are single-cellular organisms that go through logarithmic and stationary growth phase (L-phase and S-phase)^{14,15}. While L-phase cells contain higher amounts of PBPs and exhibit high photosynthetic efficiency^{14,15}, cells in S-phase are characterized by greatly reduced amount of PBPs¹⁴. The cryptophyte cells may regulate their light-harvesting capability via utilizing a specialized antenna system according to their particular growth phase. The recently determined structures of PSI-ACPI from *Chroomonas placoidea* (CpPSI-ACPI) provide a basis for understanding the assembly and pigment arrangement of CACs in cryptophyte PSI at L-phase¹². However, the precise details of how the antennae of PSI are organized at S-phase remain unknown.

Here, we solved four structures of cryptophyte PSI-CAC complexes purified from *Rhodomonas salina* (*Rs*) cells grown at L- and S-phase. Comparison of the four structures reveals how cryptophytes adjust their PSI antennae in response to the different growth state. Our results provide structural basis for detailed understanding of the regulatory mechanism of photosynthetic organisms to cope with the environmental stresses.

Results

Overall structure of PSI-CACs

We cultured cryptophyte *Rhodomonas salina* (*Rs*) cells in F/2 medium¹⁶ and measured their growth curve by continuously counting the cell number for 13 days. Our result showed that *R. salina* cells first grow exponentially and

¹Key Laboratory of Biomacromolecules (CAS), National Laboratory of Biomacromolecules, CAS Center for Excellence in Biomacromolecules, Institute of Biophysics, Chinese Academy of Sciences, Beijing, China. ²University of Chinese Academy of Sciences, Beijing, China. ³These authors contributed equally: Shumeng Zhang, Long Si. ✉e-mail: meili@ibp.ac.cn

then enter the S-phase at the 9th day (Supplementary Fig. 1a). Moreover, we found that *R. salina* cells at S-phase showed reduced absorption at 545 nm (Supplementary Fig. 1b), indicating that the amount of PE545 (PBP in *R. salina*) decreases in S-phase cells. These observations are in agreement with previously reported results^{14,17,18}. The *R. salina* cells grown for six and 12 days (corresponding to L-phase and S-phase) were harvested, and utilized to isolate PSI-CAC complexes. We then solved four structures of PSI-CAC complexes purified from cells in both growth phases, containing either 14 or 11 CACs, and termed them as PSI-14CAC_{L-phase} and PSI-11CAC_{L-phase} for L-phase models, and PSI-14CAC_{S-phase} and PSI-11CAC_{S-phase} for S-phase models (Figs. 1–2, Table 1, Supplementary Figs. 1–6).

Two PSI-14CAC structures closely resemble each other, containing 14 CAC subunits which encircle the core complex. The 14 CACs were named CAC-a to CAC-n in a clockwise direction when looked at the luminal side (Figs. 1–2). Eleven CACs (CAC-a to CAC-k) constitute the inner antenna layer surrounding the core as a closed ring, whereas CAC-l/m/n form the outer layer covering CAC-a/b/c. One subunit (termed chain-s) contains one transmembrane helix and binds three Chl a, two Chl c2 and three α -carotene molecules (Supplementary Figs. 6a, 7a). Chain-s is sandwiched by the inner CAC-a/b/c and the outer CAC-l/m/n (Fig. 1), and forms multiple hydrogen bond interactions with CAC-a/b/l/m and PsaF (Supplementary Fig. 7b, c). The only difference between the two PSI-14CAC structures is that in the PSI-14CAC_{L-phase} complex, one four-helix-bundle protein situates at the luminal side, while in the PSI-14CAC_{S-phase} structure, it appears to be missing (Figs. 1–2). Based on our high-quality cryo-EM map and transcriptome sequencing results (Supplementary Fig. 6b, c), we determined the identity of the lumen-localized protein, which is an uncharacterized yet highly conserved protein in cryptophytes (Supplementary Fig. 8). The overall folding of this protein is similar to the PSII extrinsic subunit PsbQ

(Supplementary Fig. 9). In addition, with the exception of PsaQ, names from PsaA to PsaS have been previously assigned to PSI subunits^{19–21}; we therefore termed it PsaQ in alphabetical order.

Except CAC-a and CAC-h, all CACs are grouped as four heterotrimers. Consistent with the trimeric organization of CACs, both PSI-11CAC structures lack one CAC trimer, but at distinct positions (Fig. 2). PSI-11CAC_{L-phase} loses the inner trimer-e/f/g which attaches to PsaO, whereas PSI-11CAC_{S-phase} lacks the outer trimer-l/m/n, which links to the inner layer through chain-s. Accordingly, PsaO is untraceable in the PSI-11CAC_{L-phase} structure, and chain-s is absent in our PSI-11CAC_{S-phase} structure. While PsaQ is also absent in our PSI-11CAC_{S-phase} structure, it binds to PSI-11CAC_{L-phase} at the same luminal position as that in PSI-14CAC_{L-phase} (Fig. 2).

Structural features of *R. salina* CACs

We identified all fourteen CAC proteins in our structures, based on our cryo-EM density and transcriptome sequencing analysis (Supplementary Fig. 10). All CACs adopt the same overall folding, containing three transmembrane helices termed helix B, C and A from the N- to C-terminus. It is noteworthy that CAC-h constitutes a RedCap (red lineage chlorophyll a/b-binding-like protein)²², and exhibits slightly different conformation and binds fewer pigment molecules compared to canonical CACs which possess 11–15 chlorophylls and five carotenoids (Supplementary Fig. 11, Supplementary Table 1). CAC-a is located slightly distant from CAC-b, as the N-terminal loop of chain-s separates the two CACs at the stromal side (Fig. 1). The remaining 12 CACs form four well-superposed trimers. CACs at equivalent positions in four trimers display high similarities in both protein folding and pigment arrangement, whereas CACs at different positions within the same trimer showing their respective characteristics (Fig. 3a, b, Supplementary Fig. 10). Specifically, the first CACs (CAC-b/e/i/l)

Fig. 1 | Overall structure of the PSI-14CAC_{L-phase} complex. Density map of *Rs*PSI-14CAC_{L-phase} complex viewed from different sides. For clarity, CACs are labeled as one letter with “CAC” being omitted.

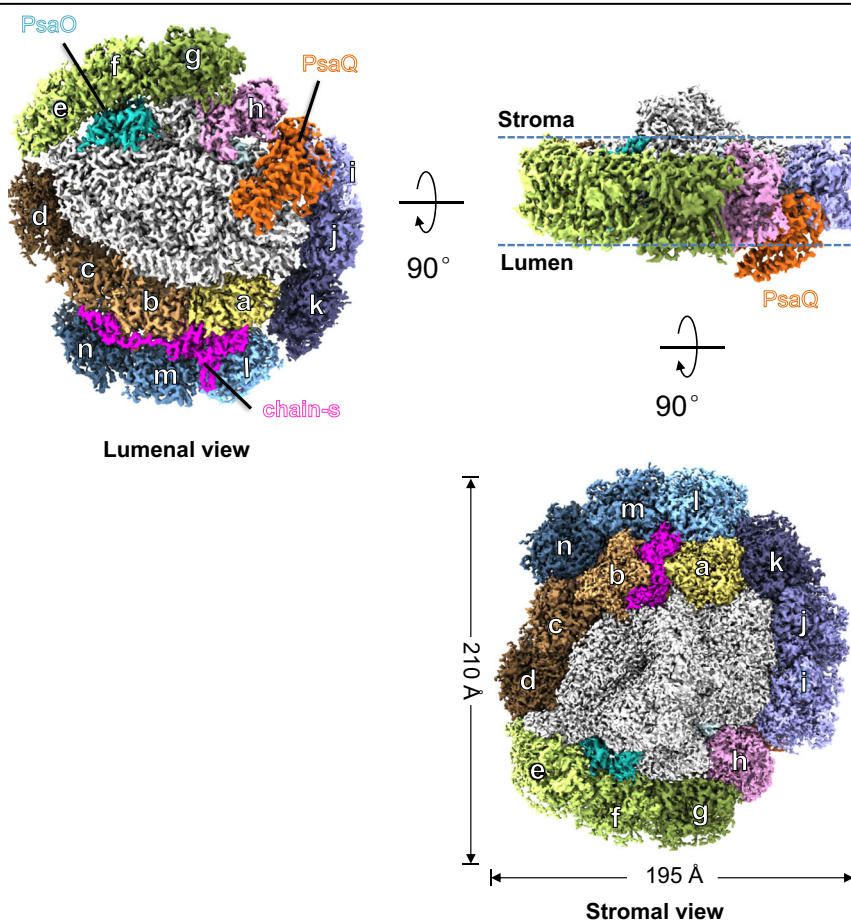
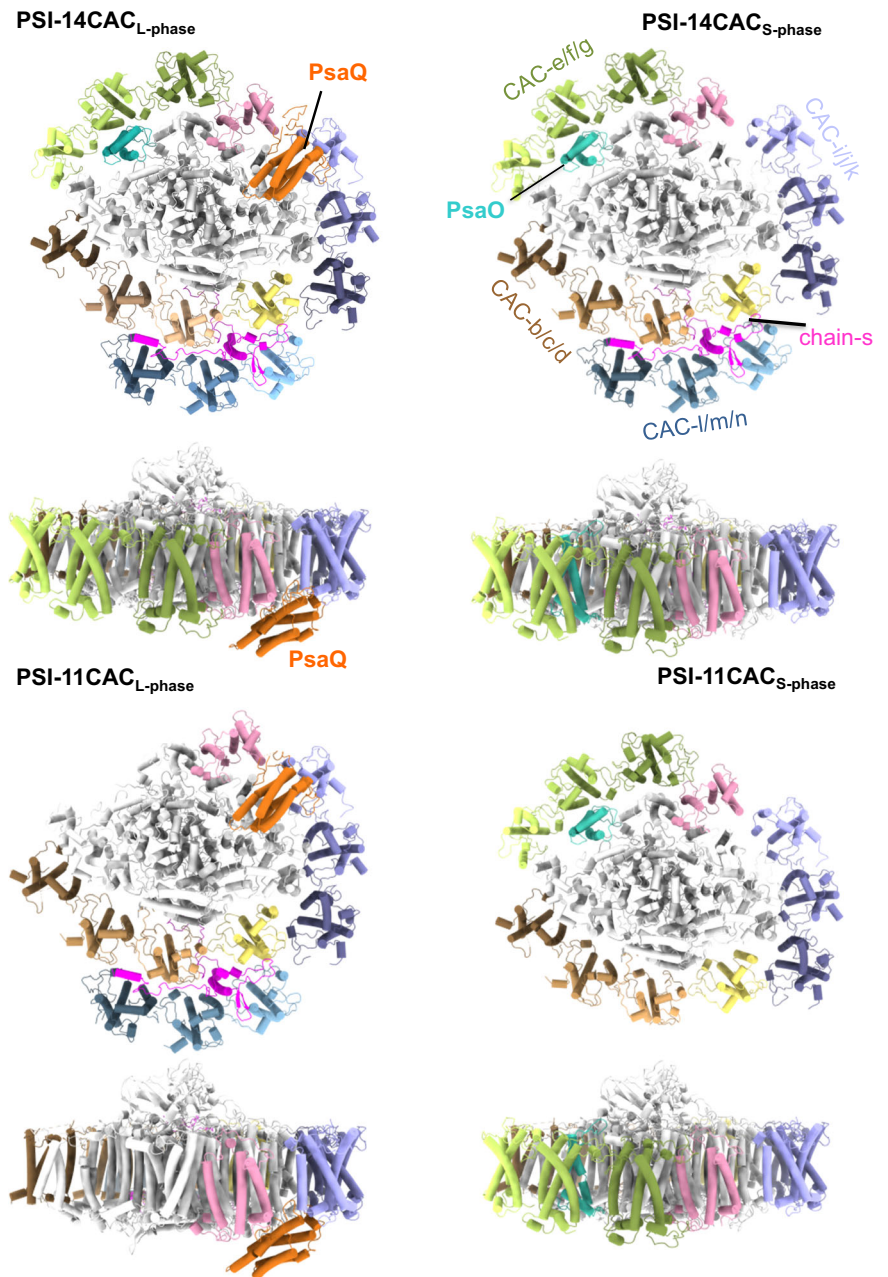


Fig. 2 | Structures of four types of *Rs*PSI-CAC complexes. Structures are viewed from the luminal side and the membrane plane, respectively. Four CAC trimers as well as PsaO and chain-s are labeled in PSI-14CAC_{S-phase} structure, whereas PsaQ is indicated in the PSI-14CAC_{L-phase} structure. The color code is the same as in Fig. 1.



possess a shorter and straight helix C, whereas the other two CACs in these trimers have a longer helix C which is bent at the stromal end. One conserved residue E/Q located at the stromal end of helix C in the second and third CACs is hydrogen-bonded with the residue on the N-terminal loop of the first and second CACs, respectively (Fig. 3a, c). In comparison, this hydrogen bond interaction is lost in the first CACs as the stromal end of their helix C is unwinding. As a result, the first CACs possess a longer AC loop (the loop between helix C and A), which extends toward the interior of the complex, attaching the CAC trimers to the core or the inner CACs (Fig. 3d). Thus, the first CACs in the trimer contribute to the inter-trimer or core-CAC interactions, whereas other two CACs participate in the intra-trimer interactions (Fig. 3d). Interestingly, we found that the second CACs in three CAC trimers (CAC-f/j/m) are identical, whereas CAC-c is a distinct protein. Structural comparison of the two CACs in the second position (CAC-c and CAC-f) showed that one chlorophyll (Chl 605) is present in CAC-f, but absent in CAC-c. Our structural superposition showed that this chlorophyll will clash with the C-terminal helix of chain-s if it binds to

CAC-c (Supplementary Fig. 12). Together, our structural observations suggested that the assembly of a CAC trimer may be initiated at the second CAC, which further recruits the first and third CAC based on their respective structural features. While the first CACs facilitate the assembly of trimers into the complex, they are unable to bind additional CAC, resulting in the trimer formation. Distinct CAC trimers occupy specific positions of the complex, which is likely a result of evolutionary selection.

All CACs and chain-s exhibit high similarities with the corresponding subunits in *Cp*PSI-ACPI structure (Supplementary Table 1, 2), in terms of the protein structure, as well as the pigment composition and arrangement. However, we also observed small structural differences between the two complexes (Supplementary Figs. 13, 14, Supplementary Table 1). For example, compared to the corresponding ACPI (ACPI-3), CAC-b in our structure contains a longer C-terminal tail which harbors an additional chlorophyll (Chl 618). The Chl 618 is positioned in the center of a three-chlorophyll-cluster which is formed by PsaA-805, PsaJ-107 and CAC-c-609 (Supplementary Fig. 14a), thus is pivotal for the efficient energy transfer

Table 1 | Cryo-EM data collection, refinement and validation statistics

	PSI-14CAC _{L-phase} (EMDB37642) (PDB 8WM6)	PSI-11CAC _{L-phase} (EMDB37654) (PDB 8WMJ)	PSI-14CAC _{S-phase} (EMDB37659) (PDB 8WMV)	PSI-11CAC _{S-phase} (EMDB37660) (PDB 8WMW)
Data collection and processing				
Magnification	130,000	130,000	130,000	130,000
Voltage (kV)	300	200	300	300
Electron exposure (e ⁻ /Å ²)	60	60	60	60
Defocus range (μm)	1.2–2.3	1.2–2.2	1.2–2.2	1.2–2.2
Pixel size (Å)	1.04	1	1.04	1.04
Symmetry imposed	C1	C1	C1	C1
Initial particle images (no.)	345,634	326,979	281,821	427,894
Final particle images (no.)	86,231	41,093	42,423	31,215
Map resolution (Å) FSC threshold	0.143	0.143	0.143	0.143
Map resolution range (Å)	2.5–3.7	2.6–4.2	2.8–4.0	3.0–4.2
Refinement				
Initial model used (PDB code)	6LY5, 5ZGB	PSI-14CAC _{L-phase}	PSI-14CAC _{L-phase}	PSI-14CAC _{L-phase}
Model resolution (Å) FSC threshold	0.143	0.143	0.143	0.143
Model resolution range (Å)	2.7	3.0	2.9	3.3
Map sharpening <i>B</i> factor (Å ²)	-57	-76	-55	-76
Model composition				
Non-hydrogen atoms	61,164	52,744	59,342	51,054
Protein residues	5216	4540	5017	4350
Ligands	415	349	407	342
<i>B</i> factors (Å²)				
Protein	23.85	16.29	30.52	33.63
Ligand	27.15	20.44	38.29	41.28
R.m.s. deviations				
Bond lengths (Å)	0.008	0.011	0.011	0.010
Bond angles (°)	1.452	1.601	1.737	1.492
Validation				
MolProbity score	1.85	1.82	1.69	1.73
Clashscore	7.88	9.45	6.38	7.19
Poor rotamers (%)	1.93	1.88	1.48	2.21
Ramachandran plot				
Favored (%)	96.82	97.48	96.65	97.65
Allowed (%)	3.11	2.52	3.33	2.33
Disallowed (%)	0.08	0.00	0.02	0.02

between the PSI core and CAC antennae. Moreover, CAC-n in our structure has one chlorophyll less than the corresponding ACPI (ACPI-9). When we compared the two structures, we found that the absence of this chlorophyll (Chl 614 in ACPI-9) is due to the steric hindrance of the C-terminal tail and one alloxanthin (Alx620) in CAC-n (Supplementary Fig. 14b). These structural differences may reflect the fine-tuning of light harvesting and energy transfer between different cryptophyte species.

PsaQ structure and interactions with neighboring subunits

PsaQ contains four helices and harbors two chlorophyll molecules (Fig. 4a). One chlorophyll (Chl a323) is coordinated by the C-terminal residue N234, while the other (Chl a322) is presumably coordinated by a water molecule (Supplementary Fig. 6b). PsaQ possesses a long loop between helix 2 and 3 (2/3-loop) which, together with the two chlorophylls, inserts into the membrane plane at the interfacial region between CAC-i and PsaB (Fig. 4b). Moreover, the N-terminal fragment of PsaQ fills in the gap between CAC-i

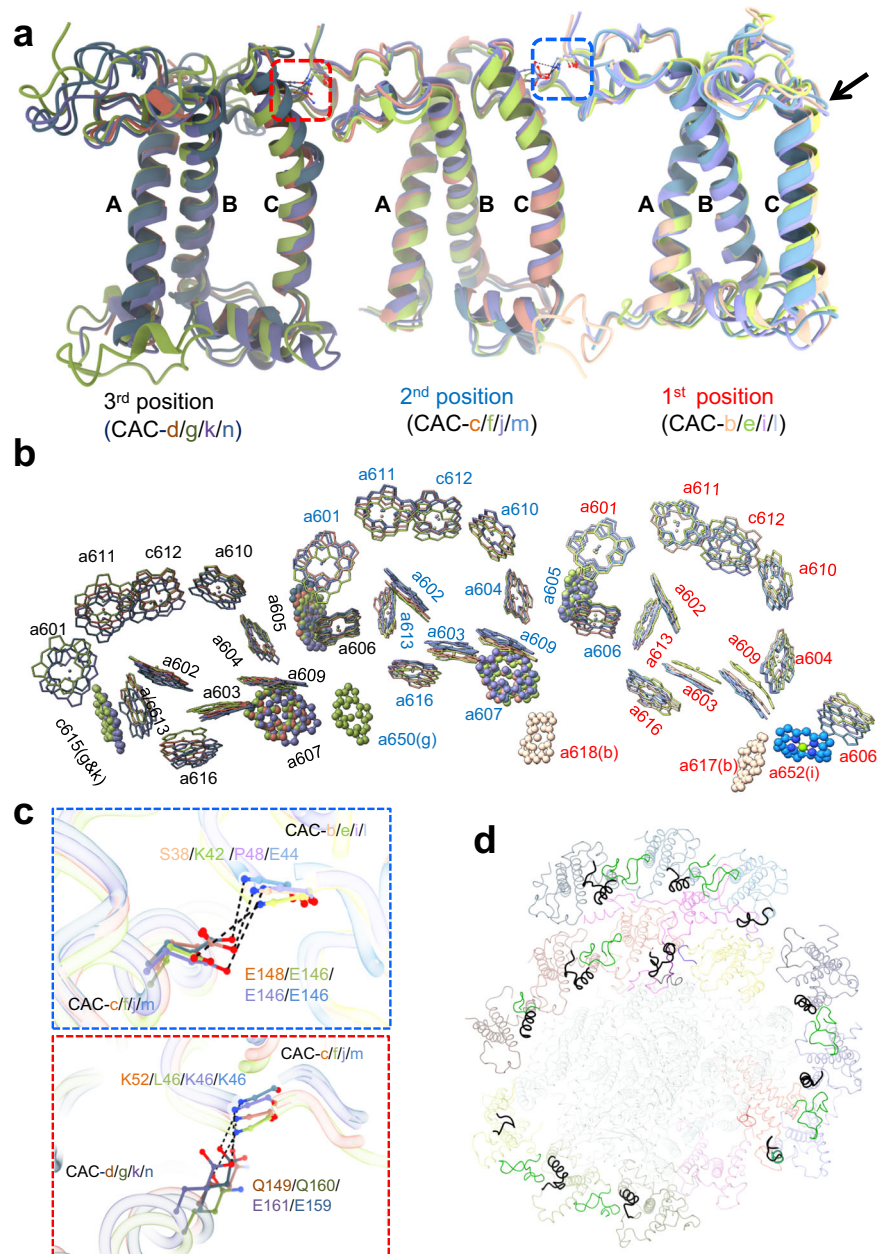
and CAC-h (Fig. 4b, c). Multiple hydrogen bond interactions between PsaQ and CAC-i/PsaB (Fig. 4d, e) tether the PsaQ protein to the lumen surface of thylakoid membrane.

While the two L-phase structures contain PsaQ, we did not observe the density corresponding to PsaQ in our two S-phase structures. Moreover, the two CpPSI-ACPI complexes purified from L-phase cells exhibited structures almost identical to our two L-phase PSI-CAC structures, and appeared to contain the lumen-localized PsaQ (Unk1 in CpPSI-ACPI)¹² (Supplementary Fig. 15, Supplementary Table 2). Together, these results suggested that PsaQ is strongly associated with the PSI-CAC complex in L-phase cells, but does not or only loosely bind to the PSI-CAC in S-phase cells.

Several chloroplast proteins with PsaQ-like folding (Supplementary Fig. 9) were found binding to the lumen surface of photosynthetic supercomplexes, and were suggested to facilitate the assembly, folding, stabilization of these supercomplexes²³. Nevertheless, a pigment-bound PsaQ-like protein has never been identified in phototrophs. PsaQ is unique to

Fig. 3 | Trimeric organization of CAC.

a, b Superposition of CAC apo-proteins (**a**) and chlorophyll (**b**) of four CAC trimers. The black arrow in (**a**) indicates the stromal end of helix C in the first CACs. **c** Specific interaction between neighboring CACs in the trimer, shown in zoom-in views of the regions encircled by boxes in (**a**). **d** Different conformation of helix C and AC loop regions adopted by CACs in four trimers. The longer AC loop in the first CACs and the corresponding region in the second and third CACs are colored in black. The N-terminal fragment of the first and second CACs involved in the interaction with helix C of neighboring CACs are in green color.



cryptophytes and the chlorophyll-coordinating residue N234 is extremely conserved in PsaQ homologs (Supplementary Fig. 8), suggesting that PsaQ and the bound chlorophylls are crucial for the proper functioning of cryptophyte cells during L-phase. Our structure showed that Chls a322/a323 of PsaQ are in close proximity to Chls a616/a606 in CAC-i and Chl a816 in PsaB (Fig. 4f). These structural observations suggest that in L-phase cells, PsaQ may facilitate efficient excitation energy transfer (EET) in PSI-CAC. In comparison, the fact that PsaQ is absent from (or loosely bound to) PSI-CAC in S-phase cells is in line with the idea that photosynthesis is less efficient in S-phase cells^{14,24}.

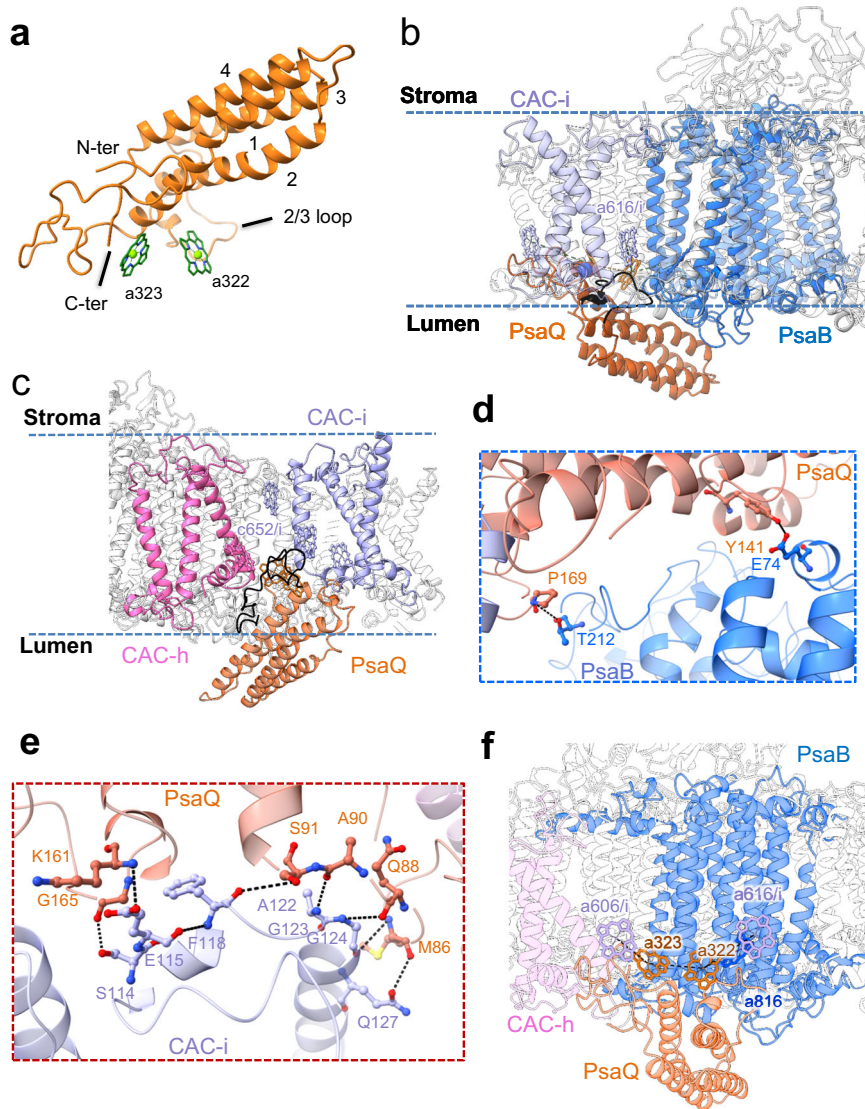
Structural comparison of RsPSI-CAC with red algal PSI-LHC

Cryptophytes were suggested to be evolutionarily originated from red algae^{7,25}, which contain LHC (also termed LHCR) proteins serving as the PSI antennae. We thus compared our PSI-CAC structures with two red algal PSI structures that are available, namely PSI-LHCR from *Cyanidioschyzon merolae* (CmPSI-LHCR) and the PSI-LHC moiety in PBS-PSII-PSI-LHC megacomplex from *Porphyridium purpureum* (PpPSI-LHC)^{5,26} (Supplementary Fig. 16). We found that CAC-i in our structure

is located more distant from the core and about 9 Å further than the corresponding LHC protein in both red algal PSI structures (Supplementary Fig. 16). In line with this observation, our cryo-EM classification result showed that CAC-i exhibits slightly lower occupancy (ranging from 62% – 90%) in all four PSI-CAC structures. The wider gap between CAC-i and the core in RsPSI-CAC complex is pivotal for the binding of PsaQ (Fig. 4b), which has been evolved only in cryptophytes. These structural observations indicated that PsaQ plays a crucial role in accomplishing cryptophyte-specific functions.

Interestingly, we found that PsaQ and PE545 share several similar features, including their exclusive presence in cryptophytes¹¹ and their luminal localization^{11,24}. In addition, compared with S-phase cells, PsaQ is more strongly associated with the PSI core (Fig. 2) and BCPs are more abundant (Supplementary Fig. 1b) in L-phase cells^{14,18,27}. These data suggest that PsaQ might be co-evolved with PE545 and assist its proper function. Our structural comparison showed that compared with CmPSI-LHCR, PpPSI-LHC is superposed better with the corresponding part of our RsPSI-CAC structures (Supplementary Fig. 16). In addition, previous report suggested that PE545 funnels the excitation energy to both photosystems²⁸,

Fig. 4 | PsaQ structure and the interactions with PSI-CAC. **a** Overall structure of PsaQ. Four helices are labeled in numbers. The N- and C-terminus (N-ter and C-ter), the loop between helix 2 and 3 (2/3 loop), and two chlorophylls are indicated. **b**, **c** PsaQ and its chlorophyll molecules insert into the membrane plane between PsaB and CAC-i (**b**) and between CAC-i and CAC-h (**c**). The 2/3 loop and N-terminal fragment of PsaQ are highlighted in black. **d**, **e** Hydrogen-bond interactions between PsaQ and PsaB (**d**) and between PsaQ and CAC-i (**e**). **f** Closely associated chlorophylls in PsaQ, PsaB and CAC-i. The protein skeleton of CAC-i is omitted for clarity.



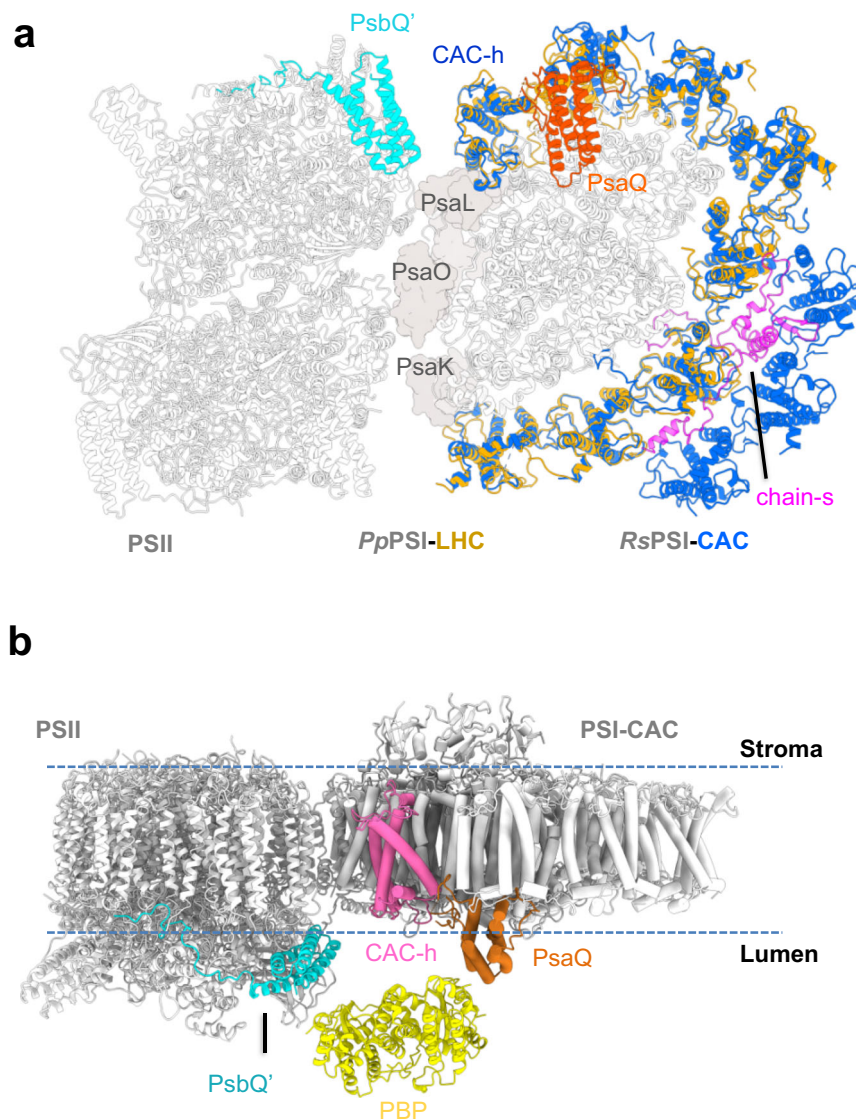
thus we hypothesize that *R. salina* PSII and the PsaQ-bound PSI may assemble into PSI-PSII megacomplex similar to that in *PpPBS*-PSII-PSI-LHC structure. The potential *RsPSI*-PSII megacomplex may form a docking site for binding PE545. When we assessed the *PpPBS*-PSII-PSI-LHC megacomplex structure for features of PSI-PSII association, we found that the PSI interacts with the PSII core through the PsaL-PsaO-PsaK side (Fig. 5a). *RsPSI*-11CAC_{L-phase} and *CpPSI*-11ACPI structures also feature an exposed PsaL-PsaO-PsaK side without bound CACs (Supplementary Fig. 15a), implying that a similar PSII-PSI-CAC megacomplex is present in the L-phase cryptophyte cells. We thus superposed our PSI-11CAC_{L-phase} structure onto the PSI part in *PpPBS*-PSII-PSI-LHC structure, generating a hypothetical *RsPSII*-PSI-CAC model (Fig. 5a).

Our hypothetic *RsPSII*-PSI-CAC model showed that the arrangement pattern of PsaQ and the PSII luminal subunit PsaQ' is almost symmetrical (Fig. 5a). Together with the membrane-embedded CAC-h, these subunits shape a luminal shallow groove with the width of ~78 Å. The PE545 is a tetramer characterized by a pseudo-two-fold symmetry, with a dimension of ~75 Å × 60 Å × 45 Å³. These features enable PE545 to fit into the luminal groove, resulting in the hypothetical model of *RsPE545*-PSII-PSI-CAC (Fig. 5b). Nevertheless, it is also possible that PE545 may be located distantly from the thylakoid membranes and the *RsPE545*-PSII-PSI-CAC is not stable in vivo. To confirm the hypothetic *RsPE545*-PSII-PSI-CAC model, further experimental evidences are required.

Discussions

Our structures presented here revealed that cryptophytes possess various types of PSI-CAC complexes. Additionally, the PSI-11CAC complexes exhibit different organization of peripheral antennae at particular growth phases. Moreover, our *RsPSI*-CAC and previously reported *CpPSI*-ACPI structures all showed that a cryptophyte-specific protein PsaQ, stably binds to the PSI-CAC complex in L-phase, but is only loosely associated with or even detaches from the PSI-CAC in S-phase cells. Based on our structural data, we speculated that PsaQ may assist the EET of PSI-CAC_{L-phase} complexes, which is in line with the previous report that L-phase cells show higher photosynthetic efficiency¹⁴. In addition, we also suggested that PsaQ is involved in binding PE545, based on the fact that PsaQ and PE545 share similar characteristics. PE545 is the soluble antenna that situates in the thylakoid lumen of cryptophytes. While previous results suggested that PE545 is able to transfer excitation energy to both photosystems^{38,29}, precisely where PE545 is positioned relative to PSI and PSII remains unknown. Direct binding of PE545 to the PSII core appears to be sterically hindered by the presence of extrinsic subunits PsaO/PsaU/PsaV and the lumen-extruding domains of PSII core subunits CP43/CP47. Furthermore, the central region of PSI core constitutes the docking site for the luminal electron donor, which may interfere with the association of PE545 with the PSI core. While direct evidence remains absent, we assume that the *RsPSII*-PSI-CAC megacomplex similar to the *PpPSII*-PSI-LHC is present in

Fig. 5 | The hypothetical *Rs*PE545-PSII-PSI-CAC model. **a The hypothetical *Rs*PSII-PSI-CAC model through superimposing *Rs*PSII-11CAC_{L-phase} structure onto the PSI-LHC moiety of *Pp*PSII-PSI-LHC megacomplex structure. **b** The hypothetical binding site of PBP (represented by PE545, PDB code 1QGW) to the PSII-PSI-CAC megacomplex in cryptophytes.**



L-phase cryptophyte cells, based on our structural observation that *Rs*PSII-11CAC_{L-phase} and *Pp*PSI-LHC resemble each other, and on the previous suggestion that cryptophytes and red algae are evolutionarily related^{8,25}. The *Rs*PSII-PSI-CAC megacomplex and PsaQ may provide a platform for binding lumen-localized PBPs, and chlorophylls in PsaQ and CACs could ensure the excitation energy harvested by PBPs being transferred to the core, as shown by our hypothetical *Rs*PE545-PSII-PSI-CAC megacomplex model. This model is in agreement with an earlier suggestion that PE545 transfers the energy to photosystems through CACs^{30,31}. Moreover, our model explains previous data measured by the steady-state and time-resolved fluorescence anisotropy, showing that PBPs funnel the excitation energy to both photosystems with similar efficiency^{28,29}. Based on our hypothetical model, the *Rs*PE545-PSII-PSI-CAC megacomplex may also serve to balance the energy distribution between the two photosystems in the *R. salina* cells at the logarithmic growth phase.

Previous results demonstrated that different types of PBPs, namely PE545 and PC645, show highly similar overall structure^{9,10}. Thus, a similar megacomplex of the PBP-PSII-PSI-CAC may be ubiquitously present in various cryptophyte species. In addition, we assumed that the proposed PBP-PSII-PSI-CAC megacomplex is more abundant in L-phase cells, as it may meet the energy requirement for the quick growth of L-phase cells. When cryptophytes enter the S-phase, changes of physiological conditions inside the chloroplast, such as lumen pH values, may weaken interactions

between PsaQ and PsaB/CAC-i, resulting in the detachment of PsaQ and the reorganization of the antennae of both photosystems. It is likely that PSI-11CAC_{L-phase} constitutes the preferential form for the potential *Rs*PE545-PSII-PSI-CAC megacomplex formation, whereas other populations of PSI-CAC complexes simultaneously exist in the chloroplast, where they may facilitate the dynamic regulation of light harvesting of PSI under different physiological conditions.

In conclusion, the findings of our study should allow to propose a regulatory mechanism by which *R. salina* adjust the light-harvesting capability and photosynthetic efficiency in line with their growth phase, namely through changing the types of antennae used as well as through rearranging the PSI-associated CACs. Future structural and biochemical assessment of the proposed *Rs*PE545-PSII-PSI megacomplex will provide detailed information required for verifying our hypothesis.

Materials and method

Cell culture and growth phase identification

R. salina cells (CCMP1319) were obtained from Provasoli-Guillard National Center for Marine Algae and Microbiota (NCMA), and cultured in F/2 medium³². The cells were bubbled with air and cultured over a period of 13 days with continuous light of 40–50 $\mu\text{mol photons/m}^2/\text{s}$. To identify the growth phase of *R. salina* cells, the number of cells were counted under microscope (Leica DM IL) equipped with 40 x objective lens every day. The

growth curve indicated that *R. salina* cells enter stationary growth phase at the 9th day (Supplementary Fig. 1a).

Purification and characterization of PSI-CAC complexes

The cells in the logarithmic (cultured for 6 days) and stationary (cultured for 12 days) growth phase were harvested through centrifugation (4500 g, 6 min) separately. Thylakoid membranes were prepared as described by Chua et al. with slight modification³³. Cells were suspended in buffer A (20 mM HEPES pH 7.5, 10 mM MgCl₂·6H₂O, 10 mM CaCl₂·2H₂O, 10 mM NaCl) and broken using a pre-chilled French press at 750 bar. The homogenate was centrifuged at 2000g for 3 min, and the supernatant was further ultra-centrifuged at 70,000 g × 40 min at 4 °C to collect the thylakoid membranes (pellets). To purify the PSI-CAC complex, thylakoid membranes were suspended in buffer A to a final concentration of 0.6 mg/ml in chlorophyll. Dodecyl- α -D-maltoside (α -DDM, 10%) was added to the suspended thylakoids to a final concentration of 1.0%. The mixture was incubated on ice for 15 min, and then centrifuged at 13,800 g, 4 °C for 10 min. The supernatant was loaded on the top of a tube containing buffer A, 0.02% α -DDM and a continuous sucrose density gradient (from 5% to 30%), and fractionated by ultra-centrifugation at 198,200 g for 18 h (Beckman SW41 rotor). The band corresponding to the PSI-CAC complex was divided into the upper half and the lower half, which were collected separately (Supplementary Fig. 1c), and further identified as PSI-11CAC and PSI-14CAC. The PSI-CAC samples were concentrated to about 1.5 mg ml⁻¹ in chlorophyll for cryo-EM specimen preparation. The protein composition of PSI-CAC samples used for cryo-EM analysis was identified by sodium dodecylsulfate polyacrylamide gel electrophoresis (SDS-PAGE) and mass spectrometry (Supplementary Fig. 1e).

Absorption spectra measurement

Absorption spectra of *R. salina* cells and the purified PSI-CAC complexes were measured by UV-Vis spectrometer U3900 (HITACHI). While the content of PBP decreases in *R. salina* cells at stationary growth phase as shown in Supplementary Fig. 1b, the four types of PSI-CAC complexes are almost identical in their absorption spectra (Supplementary Fig. 1d).

Pigment composition of PSI-CAC complex

Pigment composition was analyzed by high-performance liquid chromatography (HPLC, LC-20AT) apparatus with a prominence fluorescence detector RF20A (Shimadzu, Japan), using a C18 reversed-phase column (Shimadzu, Japan). We assumed that all four types of PSI-CAC complexes have similar pigment composition since they exhibit almost identical absorption spectra. We therefore only analyzed the PSI-14CAC_{L-phase} sample. The complex sample collected from the sucrose density gradient was concentrated to 1.5 mg ml⁻¹ (in chlorophyll) and mixed with 90% (v/v) cold acetone. The mixture was centrifuged at 13,000 g for 10 min to extract pigment molecules²⁰. The supernatant containing pigments was loaded on the C18 reversed-phase column (Shimadzu, Japan) and eluted at 20 °C at a flow rate of 1 ml/min with the following steps: 1–20 min, linear gradient of buffer A (acetonitrile: water at the ratio of 85 : 15) from 100% – 0%; 20–23 min, 100% buffer B (ethyl acetate); 23–24 min, linear gradient of buffer B from 100% – 0%; and 24–28 min, 100% buffer A. The eluent was detected at 440 nm with a wavelength detection range of 300–800 nm. Pigments were identified based on their characteristic absorption spectra and retention times of each peak fraction^{34,35} (Supplementary Fig. 1f).

R. salina mRNA sequencing

Fresh *R. salina* cells were harvested and stored in liquid nitrogen, then sent to Beijing Genomics Institute (BGI) for high-throughput sequencing analysis. The mRNA extraction, complementary DNA (cDNA) library construction, sequencing and bioinformatics analysis were performed by the technical staffs at BGI. Total RNA was extracted from the fresh *R. salina* cells. The mRNA was enriched by oligo (dT)-attached magnetic beads from the denatured RNA sample with the opened secondary structure. Then the mRNAs were fragmented and reversely transcript to cDNA fragments,

which were further amplified by PCR. The PCR products were denatured to obtain single-stranded DNA products, which were then cyclized and used for sequencing. A total of 10.14 Gb data were sequenced in this project. The raw data was filtered with SOAPnuke (v1.6.5)³⁶ to obtain clean reads, which was then assembled by Trinity v2.0.6³⁷. Clean data were mapped to the assembled unique gene by Bowtie2 v2.2.5³⁸, and the expression level of gene was calculated by RSEM (v1.3.1)³⁹. Gene annotation was performed using seven major functional databases (NR, NT, SwissProt, KOG, KEGG, GO and Pfam). Two parallel tests yielded the same results.

Grid preparation and cryo-EM data acquisition

The PSI-CAC samples were added to a glow discharged holey carbon grid (GIG-A31213). The sample was vitrified by flash plunging the grid into liquid ethane using vitrobot Mark IV (FEI) with blotting time of 4 s, force level of 4 and humidity of 100%. The micrographs were collected using SerialEM v3.6/3.6.1 data collection software on 300 kV Titan Krios (FEI) microscope equipped with K2 direct electron detector (Gatan) (for PSI-14CAC_{L-phase}, PSI-11CAC_{S-phase} and PSI-14CAC_{S-phase}) and 200 kV Talos Arctica (FEI) equipped with K2 direct electron detector (Gatan) (for PSI-11CAC_{L-phase}). The parameters for data collection were summarized in Table 1.

Data processing

All movie stacks were corrected by program Motion Cor 2 with dose weighting⁴⁰. CTF parameters of each movie were estimated by Gctf⁴¹. Images were processed using the program RELION 3.1⁴². Automatic particle picking and reference-free 2D classifications were performed. The selected particles were used as templates for further picking procedure, then the picked particles were applied to 2D and 3D classification. After 3D non-uniform refinement and sharpening, CTF refinement (global and local) and post processing were performed. The data collection and processing procedures were summarized in Supplementary Fig. 2–5. The final overall resolutions of maps of *R. salina* PSI-14CAC_{L-phase}, PSI-11CAC_{L-phase}, PSI-14CAC_{S-phase}, PSI-11CAC_{S-phase} are 2.7 Å, 3.0 Å, 2.9 Å and 3.3 Å, respectively. Local refinement targeting the PsaQ in PSI-14CAC_{L-phase} was performed, resulting in a final local map with the resolution of 3.5 Å. The resolutions of the final maps were calculated using ResMap⁴³.

Model building, refinement and validation

For model building of the PSI-14CAC_{L-phase}, the PSI core from the cryo-EM structure of diatom PSI-FCPI (PDB code: 6LY5) was manually docked into the 2.7 Å resolution cryo-EM map using UCSF Chimera⁴⁴. The CAC antennae were built by docking a single LHCR structure from the red algal PSI-LHCR model (PDB code 5ZGB) into the cryo-EM map. The identification of each individual CAC antenna was based on the best match of the specific sequence with the cryo-EM densities. The amino acid sequences of CAC antennae were then mutated to their counterparts in *R. salina*. To identify the PsaQ protein, we first traced a short peptide containing 10 residues (¹KQRVVLGKI¹⁰) at the local helix region based on the 3.5 Å local map. We then searched the *R. salina* protein sequences derived from our transcriptome sequencing result, and found that a fragment of PsaQ (⁹⁵KQRTVLGKI¹⁰⁴) shows high similarity with the short peptide (Supplementary Fig. 6c). Based on the determined amino acid sequence of PsaQ, we manually built the PsaQ model and found that most amino acids of PsaQ fit the density well (Supplementary Fig. 6b). After the model building of PSI-14CAC_{L-phase} structure, automatic real-space refinements in Phenix⁴⁵ and manual correction in COOT⁴⁶ were carried out iteratively. The models of PSI-11CAC_{L-phase}, PSI-14CAC_{S-phase} and PSI-11CAC_{S-phase} were built by docking the corresponding part of refined PSI-14CAC_{L-phase} model into the cryo-EM maps, and then performing manual adjustment and real-space refinements. The geometries of four structures were assessed using Phenix⁴⁵ and MolProbity⁴⁷ and detailed information were listed in Table 1. The structural figures were prepared using ChimeraX 1.2⁴⁴ (Molecular Graphics System). The figure of sequence alignment was generated using ESPript65 v.3.0.

Statistics and reproducibility

The counting of *R. salina* cell numbers was performed in three biological replicates. Other experiments, including the absorption spectra measurement, SDS-PAGE and HPLC analysis were performed in 2-6 biological replicates, with reproducible results obtained.

Reporting summary

Further information on research design is available in the Nature Portfolio Reporting Summary linked to this article.

Data availability

The atomic coordinates and cryo-EM density maps of PSI-CAC complexes have been deposited in the Protein Data Bank (PDB) and Electron Microscopy Data Bank (EMDB) with accession codes: 8WM6 and EMDB-37642 for PSI-14CAC_L-phase structure, 8WMJ and EMDB-37654 for PSI-11CAC_L-phase structure, 8WMV and EMDB-37659 for PSI-14CAC_S-phase structure, 8WMW and EMDB-37660 for PSI-11CAC_S-phase structure. The locally refined cryo-EM map of PsaQ has been deposited in the EMDB with accession code EMDB-37674. RNA sequencing data have been deposited into the NCBI Sequence Read Archive (SRA) under the BioProject ID PRJNA1104392. The uncropped gel image of Supplementary Fig. 1e is provided in Supplementary Fig. 17. All other data generated or analyzed in this study is available from the corresponding author on reasonable request.

Received: 22 December 2023; Accepted: 30 April 2024;

Published online: 11 May 2024

References

1. Stadnichuk, I. N. & Kusnetsov, V. V. Phycobilisomes and phycobiliproteins in the pigment apparatus of oxygenic photosynthetic: from cyanobacteria to tertiary endosymbiosis. *Int. J. Mol. Sci.* **24**, 2290 (2023).
2. Rakhimberdieva, M. G., Boichenko, V. A., Karapetyan, N. V. & Stadnichuk, I. N. Interaction of phycobilisomes with photosystem II dimers and photosystem I monomers and trimers in the cyanobacterium *Spirulina platensis*. *Biochemistry* **40**, 15780–15788 (2001).
3. Liu, H. et al. Phycobilisomes supply excitations to both photosystems in a megacomplex in cyanobacteria. *Science* **342**, 1104–1107 (2013).
4. Gantt, E., Grabowski, B. & Cunningham, F. X. Antenna systems of red algae: phycobilisomes with photosystem II and chlorophyll complexes with photosystem. In *Light-harvesting antennas in photosynthesis* Vol 15, 307–322 (Kluwer Academics, Netherlands, 2003).
5. Pi, X. et al. Unique organization of photosystem I-light-harvesting supercomplex revealed by cryo-EM from a red alga. *Proc. Natl Acad. Sci. USA* **115**, 4423–4428 (2018).
6. Rochaix, J. D. & Bassi, R. LHC-like proteins involved in stress responses and biogenesis/repair of the photosynthetic apparatus. *Biochem. J.* **476**, 581–593 (2019).
7. Delwiche, C. F. & Palmer, J. D. The origin of plastids and their spread via secondary symbiosis. In *Plant Systematics and Evolution* Vol 11, 53–86 (Springer, Vienna, 1997).
8. Durnford, D. G. et al. A phylogenetic assessment of the eukaryotic light-harvesting antenna proteins, with implications for plastid evolution. *J. Mol. Evol.* **48**, 59–68 (1999).
9. Wilk, K. E. et al. Evolution of a light-harvesting protein by addition of new subunits and rearrangement of conserved elements: crystal structure of a cryptophyte phycoerythrin at 1.63-Å resolution. *Proc. Natl Acad. Sci. USA* **96**, 8901–8906 (1999).
10. Harrop, S. J. et al. Single-residue insertion switches the quaternary structure and exciton states of cryptophyte light-harvesting proteins. *Proc. Natl Acad. Sci. USA* **111**, E2666–E2675 (2014).
11. Ludwig, M. & Gibbs, S. P. Localization of phycoerythrin at the luminal surface of the thylakoid membrane in *Rhodomonas lens*. *J. Cell Biol.* **108**, 875–884 (1989).
12. Zhao, L. S. et al. Structural basis and evolution of the photosystem I-light-harvesting supercomplex of cryptophyte algae. *Plant Cell* **35**, 2449–2463 (2023).
13. Hoffman, G. E., Sanchez Puerta, M. V. & Delwiche, C. F. Evolution of light-harvesting complex proteins from Chl c-containing algae. *BMC Evol. Biol.* **11**, 101 (2011).
14. Cheregi, O. et al. Presence of state transitions in the cryptophyte alga *Guillardia theta*. *J. Exp. Bot.* **66**, 6461–6470 (2015).
15. Maltsev, Y., Maltseva, K., Kulikovskiy, M. & Maltseva, S. Influence of light conditions on microalgae growth and content of lipids, carotenoids, and fatty acid composition. *Biology (Basel)* **10**, 1060 (2021).
16. Kana, R., Kotabova, E., Sobotka, R. & Prasil, O. Non-photochemical quenching in cryptophyte alga *Rhodomonas salina* is located in chlorophyll a/c antennae. *PLoS One* **7**, e29700 (2012).
17. Cunningham, B. R. et al. Light capture and pigment diversity in marine and freshwater cryptophytes. *J. Phycol.* **55**, 552–564 (2019).
18. Heidenreich, K. M. & Richardson, T. L. Photopigment, absorption, and growth responses of marine cryptophytes to varying spectral irradiance. *J. Phycol.* **56**, 507–520 (2020).
19. Khrouchtchova, A. et al. A previously found thylakoid membrane protein of 14kDa (TMP14) is a novel subunit of plant photosystem I and is designated PSI-P. *FEBS Lett.* **579**, 4808–4812 (2005).
20. Xu, C. et al. Structural basis for energy transfer in a huge diatom PSI-FCPI supercomplex. *Nat. Commun.* **11**, 5081 (2020).
21. Bai, T., Guo, L., Xu, M. & Tian, L. Structural diversity of photosystem I and its light-harvesting system in eukaryotic algae and plants. *Front. Plant Sci.* **12**, 781035 (2021).
22. Engelken, J., Brinkmann, H. & Adamska, I. Taxonomic distribution and origins of the extended LHC (light-harvesting complex) antenna protein superfamily. *BMC Evol. Biol.* **10**, 233 (2010).
23. Ifuku, K. The PsbP and PsbQ family proteins in the photosynthetic machinery of chloroplasts. *Plant Physiol. Biochem.* **81**, 108–114 (2014).
24. Kana, R., Prasil, O. & Mullineaux, C. W. Immobility of phycobilins in the thylakoid lumen of a cryptophyte suggests that protein diffusion in the lumen is very restricted. *FEBS Lett.* **583**, 670–674 (2009).
25. Douglas, S. E. Eukaryote-eukaryote endosymbioses: insights from studies of a cryptomonad alga. *Biosystems* **28**, 57–68 (1992).
26. You, X. et al. In situ structure of the red algal phycobilisome-PSII-PSI-LHC megacomplex. *Nature* **616**, 199–206 (2023).
27. Yamamoto, S., Bossier, P. & Yoshimatsu, T. Biochemical characterization of *Rhodomonas* sp. Hf-1 strain (cryptophyte) under nitrogen starvation. *Aquaculture* **516**, 734648 (2020).
28. van der Weij-De Wit, C. D. et al. How energy funnels from the phycoerythrin antenna complex to photosystem I and photosystem II in cryptophyte *Rhodomonas* CS24 cells. *J. Phys. Chem. B* **110**, 25066–25073 (2006).
29. Kereiche, S. et al. Association of chlorophyll a/c(2) complexes to photosystem I and photosystem II in the cryptophyte *Rhodomonas* CS24. *Biochim. Biophys. Acta* **1777**, 1122–1128 (2008).
30. Stadnichuk, I. N. et al. Phycoerythrin association with photosystem II in the cryptophyte alga *Rhodomonas salina*. *Biochem. (Mosc.)* **85**, 679–688 (2020).
31. Sebelik, V., West, R., Trskova, E. K., Kana, R. & Polivka, T. Energy transfer pathways in the CAC light-harvesting complex of *Rhodomonas salina*. *Biochim. Biophys. Acta Bioenerg.* **1861**, 148280 (2020).
32. Guillard, R. R. & Ryther, J. H. Studies of marine planktonic diatoms. I. *Cyclotella nana* Husted, and *Detonula confervacea* (Cleve) Grun. *Can. J. Microbiol.* **8**, 229–239 (1962).
33. Chua, N. H. & Bannoun, P. Thylakoid membrane polypeptides of *Chlamydomonas reinhardtii*: wild-type and mutant strains deficient in photosystem II reaction center. *Proc. Natl Acad. Sci. USA* **72**, 2175–2179 (1975).

34. Wright, S. W. & Jeffrey, S. W. Pigment markers for phytoplankton production. *Marine organic matter: biomarkers, isotopes and DNA* **2N**, 71–104 (2006).
35. Roy, S., Llewellyn, C. A., Egeland, E. S. & Johnsen, G. *Phytoplankton Pigments: Characterization, Chemotaxonomy and Applications in Oceanography* 165–236 (Cambridge University Press, 2011).
36. Chen, Y. et al. SOAPnuke: a MapReduce acceleration-supported software for integrated quality control and preprocessing of high-throughput sequencing data. *GigaScience* **7**, 1–6 (2018).
37. Grabherr, M. G. et al. Full-length transcriptome assembly from RNA-Seq data without a reference genome. *Nat. Biotechnol.* **29**, 644–652 (2011).
38. Langmead, B. & Salzberg, S. L. Fast gapped-read alignment with bowtie 2. *Nat. Methods* **9**, 357–359 (2012).
39. Li, B. & Dewey, C. N. RSEM: accurate transcript quantification from RNA-Seq data with or without a reference genome. *BMC Bioinforma.* **12**, 323 (2011).
40. Zheng, S. Q. et al. MotionCor2: anisotropic correction of beam-induced motion for improved cryo-electron microscopy. *Nat. methods* **14**, 331–332 (2017).
41. Zhang, K. Gctf: Real-time CTF determination and correction. *J. Struct. Biol.* **193**, 1–12 (2016).
42. Scheres, S. H. RELION: implementation of a Bayesian approach to cryo-EM structure determination. *J. Struct. Biol.* **180**, 519–530 (2012).
43. Kucukelbir, A., Sigworth, F. J. & Tagare, H. D. Quantifying the local resolution of cryo-EM density maps. *Nat. Methods* **11**, 63–65 (2014).
44. Pettersen, E. F. et al. UCSF chimera—a visualization system for exploratory research and analysis. *J. Comput. Chem.* **25**, 1605–1612 (2004).
45. Adams, P. D. et al. PHENIX: a comprehensive Python-based system for macromolecular structure solution. *Acta Crystallogr. Sect. D. Biol. Crystallogr.* **66**, 213–221 (2010).
46. Emsley, P., Lohkamp, B., Scott, W. G. & Cowtan, K. Features and development of Coot. *Acta Crystallogr. Sect. D. Biol. Crystallogr.* **66**, 486–501 (2010).
47. Chen, V. B. et al. MolProbity: all-atom structure validation for macromolecular crystallography. *Acta Crystallogr. Sect. D. Biol. Crystallogr.* **66**, 12–21 (2010).

Acknowledgements

We thank B. Zhu, X. Huang, X. Li and other staff members at the Center for Biological Imaging (IBP, CAS) for their support in data collection; L. Niu for mass spectrometry; L. Shi for assisting pigment identification. We thank Torsten Juelich (University of Chinese Academy of Sciences) for linguistic assistance during the preparation of the article. The project is funded by the Strategic Priority Research Program of CAS (XDB37020101), National Natural Science Foundation of China (31930064, 32171183), the CAS

Project for Young Scientists in Basic Research (#YSBR-015) and Youth Innovation Promotion Association, Chinese Academy of Sciences (Y2022038).

Author contributions

M.L. conceived and coordinated the project; L.S. performed the sample preparation, data collection, and reconstructed the cryo-EM maps; S.Z. built and refined the structure models; X.S. helped in cryo-EM data collection; X.Z. and X.A. assisted in *R. salina* cell culturing and complex isolation; S.Z., L.S. and M.L. analyzed the structures; S.Z. and M.L. wrote the manuscript; all authors discussed and commented on the results and the manuscript.

Competing interests

The authors declare no competing interests.

Additional information

Supplementary information The online version contains supplementary material available at <https://doi.org/10.1038/s42003-024-06268-5>.

Correspondence and requests for materials should be addressed to Mei Li.

Peer review information *Communications Biology* thanks the anonymous, reviewer(s) for their contribution to the peer review of this work. Primary Handling Editors: Tobias Goris. A peer review file is available.

Reprints and permissions information is available at <http://www.nature.com/reprints>

Publisher's note Springer Nature remains neutral with regard to jurisdictional claims in published maps and institutional affiliations.

Open Access This article is licensed under a Creative Commons Attribution 4.0 International License, which permits use, sharing, adaptation, distribution and reproduction in any medium or format, as long as you give appropriate credit to the original author(s) and the source, provide a link to the Creative Commons licence, and indicate if changes were made. The images or other third party material in this article are included in the article's Creative Commons licence, unless indicated otherwise in a credit line to the material. If material is not included in the article's Creative Commons licence and your intended use is not permitted by statutory regulation or exceeds the permitted use, you will need to obtain permission directly from the copyright holder. To view a copy of this licence, visit <http://creativecommons.org/licenses/by/4.0/>.

© The Author(s) 2024